Deciphering the state of the lower crust and upper mantle with multi-physics inversion

Max Moorkamp[1]

[1]Ludwig-Maximilians-Universität, Department of Earth and Environmental Sciences, Theresienstrasse 41, 80333 Munich, Germany

In this document I provide additional information on the input datasets, the inversion runs and some sensitivity tests. Furthermore, I give an overview of additional files contained in the Supplementary material such as slices through the model along all three axes, etc.

1 Gravity data processing

The free air gravity data are extracted from the XGM2016 gravity modelPail et al. (2018) at a height of 5,000m above the geoid and thus located above the highest topography in the region. In order to overcome the strong correlation between topography and gravity signal and to enable inversion with a flat model, the topographic and bathymetric gravity signal are removed using the method outlined in Szwillus et al. (2016). Based on a filtered version of ETOPO1 matching the resolution of XGM2016 a density model covering the area where XGM2016 is evaluated extended by 5^o is constructed. The model contains the density differences between the densities assigned to topographic $\rho_{topo} = 2670\text{kg/m}^3$ and water masses $\rho_w = 1040\text{kg/m}^3$ and a reference column (see figure 1). The "Tesseroids" routines Uieda et al. (2016) are used to calculate the gravity effect of this model. Pail et al. (2018)

The same procedure is also used to remove the gravity signals of the oceanic crust and the density jump at the Moho (see figure 1). Densities of $\rho_{c,cont} = 2700kg/m^3$ and $\rho_{c,oc} = 2900kg/m^3$ for continental and oceanic crust and $\rho_m = 3200kg/m^3$ for the mantle are used, respectively. The ocean age grid by Müller et al. (2008) is used to distinguish between oceanic and continental density columns. Moho depths are taken from the model by Szwillus et al. (2019) (see figure 2). The resulting residual gravity anomaly used

Corresponding author: Max Moorkamp, `Max.Moorkamp@lmu.de`

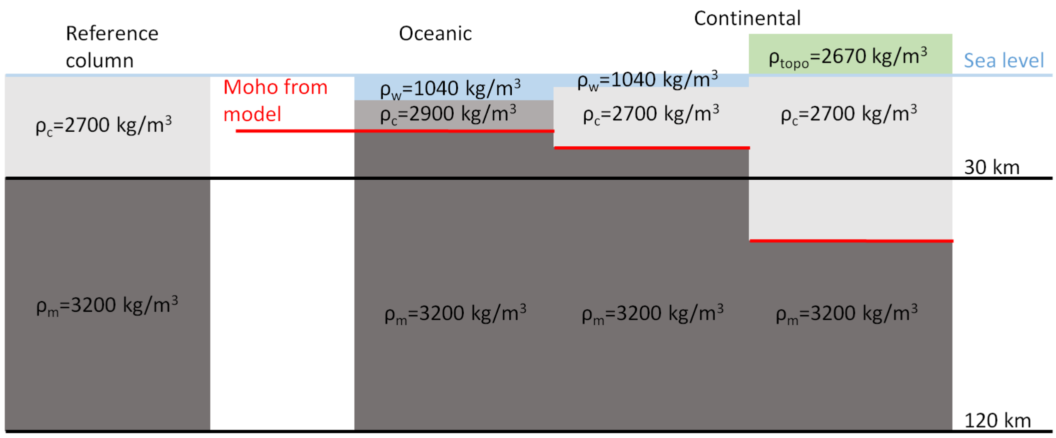

Figure 1: Sketch of the (reference) density columns used to calculate the topographic/bathymetric–, Moho– and oceanic crustal gravity effects. The topographic, water, crustal and mantle densities are denoted by ρ_{topo}, ρ_w, ρ_c and ρ_m, respectively. Note the different ρ_c for continental and oceanic areas.

in the inversions is:

$$\delta g_{res} = \delta g - (g_{tb} + g_{moho} + g_{oc}).,\tag{1}$$

where δg_{res} is the residual gravity effect and g_{tb}, g_{moho} and g_{oc} are the topographic–bathymetric, Moho and oceanic crustal gravity effects, respectively. All these gravity fields are displayed in figure 3.

I test the impact of this gravity data processing below, where I employ a different gravity dataset with a different processing and compare the results.

2 Inversion information

The inversion minimizes an objective function of the form

$$\begin{aligned}\Phi(\sigma,\rho) \quad &= \quad \lambda_1\Phi_{d,MT}(\sigma) + \lambda_2\Phi_{d,grav}(\rho) + \lambda_3\Phi_{VI}(\sigma,\rho) + \\ &\quad\quad \lambda_4\Phi_{reg,\sigma}(\sigma) + \lambda_5\Phi_{reg,\rho}(\rho).\end{aligned}$$

Here σ is the electrical conductivity, ρ density, $\Phi_{d,MT}$ and $\Phi_{d,grav}$ are the data misfit terms for magnetotellurics and gravity data, respectively, and $\Phi_{reg,\sigma}$ and $\Phi_{reg,\rho}$ the corresponding regularization terms. $\Phi_{VI}(\sigma,\rho)$ is the variation of information constraint that couples the two methods and $\lambda_1,\ldots,\lambda_5$ are weighting factors to control the influence of each term.

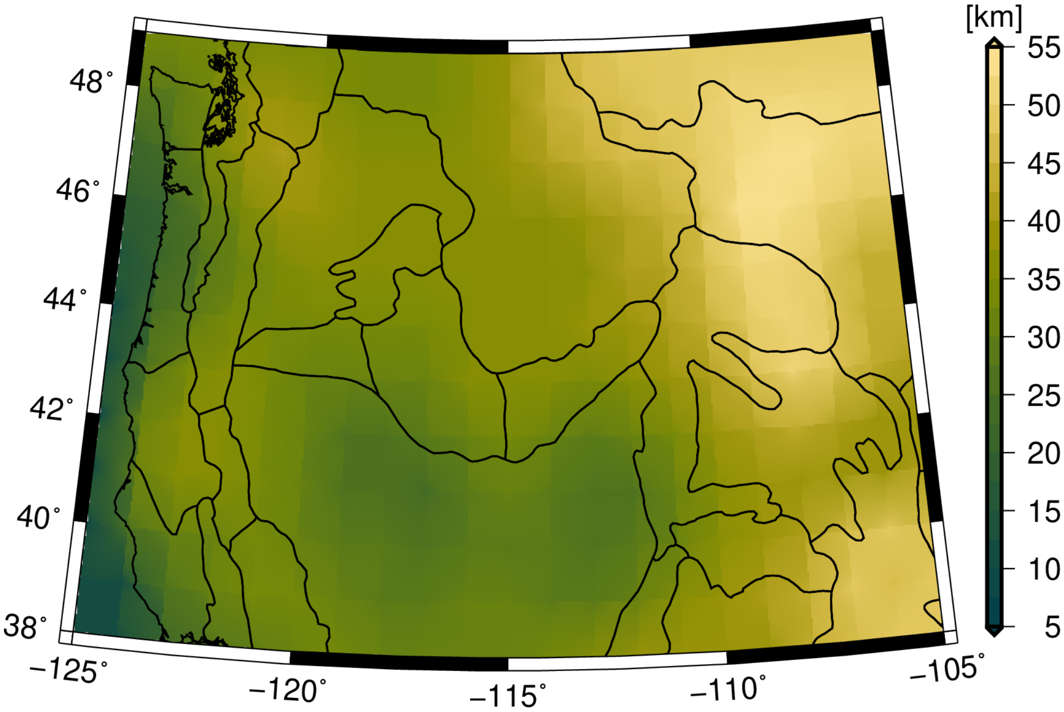

Figure 2: Depth to the Moho in the Northwestern USA from Szwillus et al. (2019).

For the inversion an error floor of 2% of the maximum absolute value of impedance in each row of the impedance tensor is assigned to the MT data. For the gravity data an error of 1-10 mGal based on the difference between a spherical approximation and a flat Earth approximation are assumed. With these errors the initial RMS values for MT and gravity are 53.3 and 25.4, respectively. I start the inversion with a high regularization value ($\lambda_4 = \lambda_5 = 10,000$ for both density and conductivity) and successively reduce this value when the inversion does not progress any further. The initial inversion iterations do not include a correction for distortion of the MT data. This feature is only enabled when the RMS for the MT data has dropped to a value of $approx10$. This strategy has been shown to be effective and robustMoorkamp et al. (2020). I keep the variation of information weight as high as possible throughout the inversion ($\lambda_3 = 10^6$ initially). However, at a later stage the inversion does not progress even when reducing the regularization weight and thus I reduce the VI weight first to $\lambda_3 = 10^5$ and finally to $\lambda_3 = 50,000$. The evolution of the different terms of the objective function in the inversion can be seen in Figure 4. Even though the convergence is slow (more than 1500 iterations) due to the non-linearity of the variation of information constraint, the data

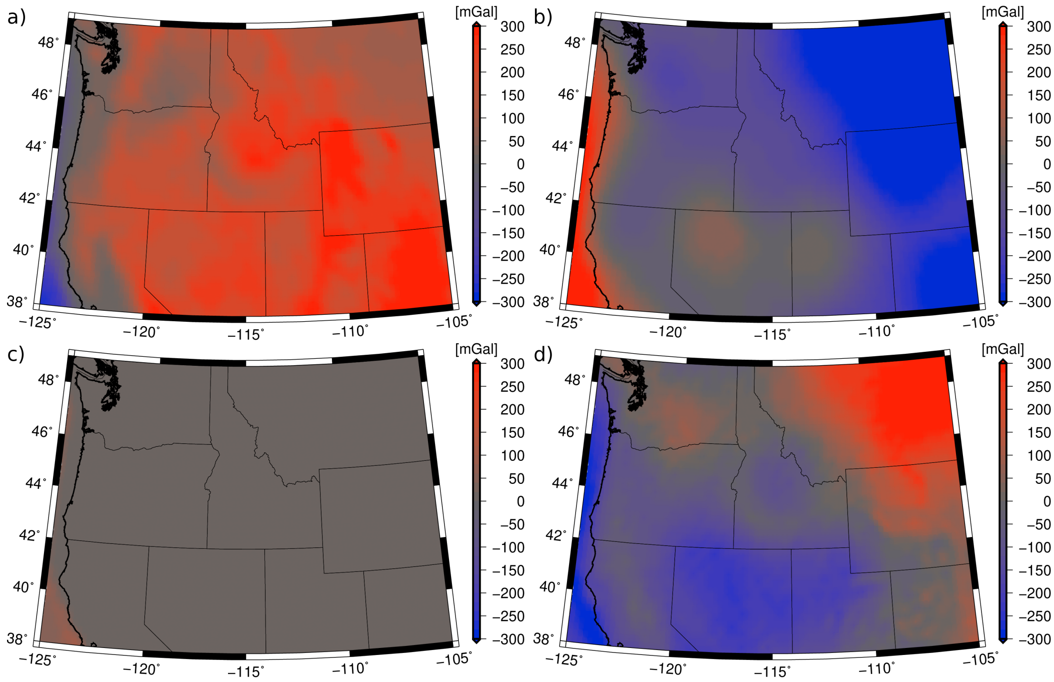

Figure 3: Gravity effects of a) topography/bathymetry, b) Moho, c) oceanic crust and d) the resulting residual gravity signal.

misfit terms for both MT and gravity converge relatively evenly to acceptable misfit values. The second half of the inversion process is largely spent on increasing the similarity between the density and conductivity structure as indicated by the near constant data misfit and decreasing VI constraint.

3 Misfit of the final inversion results

The global RMS values of the final inversion model for MT and gravity are 1.6 and 1.9, respectively, based on the error assumptions given above. However, such global misfit values can be misleading as often the distribution of misfit is heterogeneous. In such as case it is possible that insignificant aspects of the data are fit very well and the features that carry important information show significant discrepancy. I therefore provide detailed information on the distribution of misfit, additional plots with predicted and observed MT curves at each sites are found in additional files (see description at the end of this document).

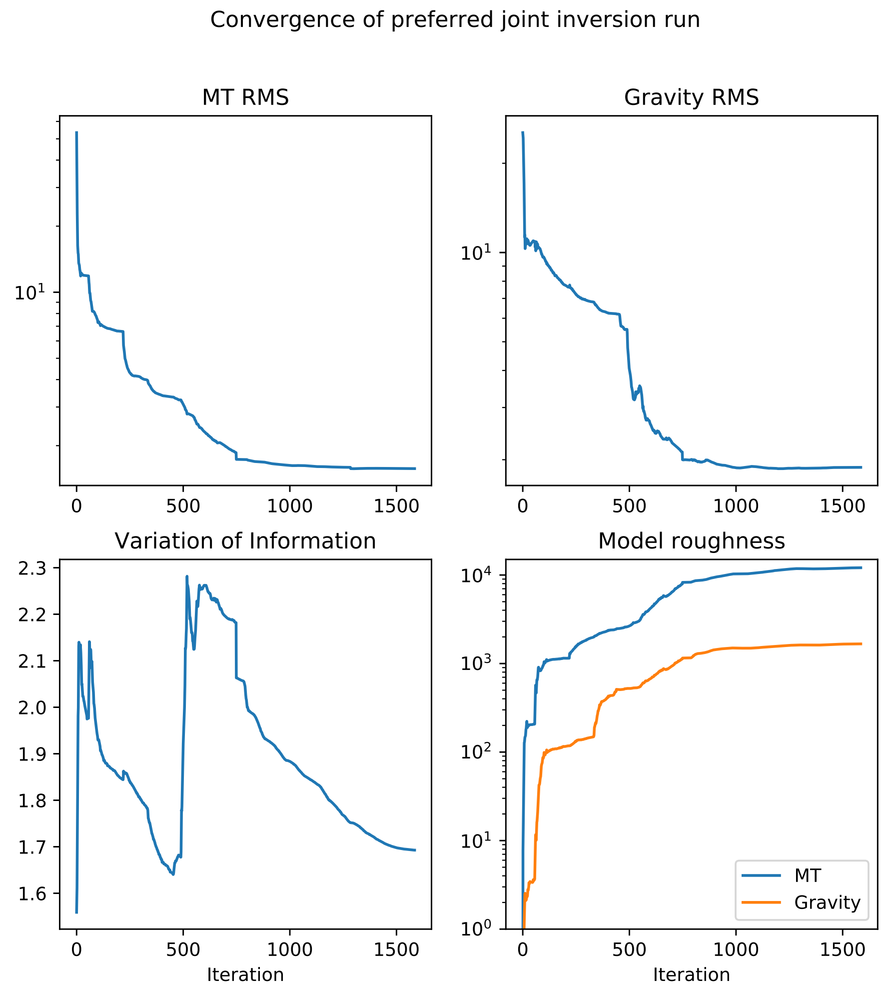

Figure 4: Evolution of the different terms of the objective function during the joint inversion.

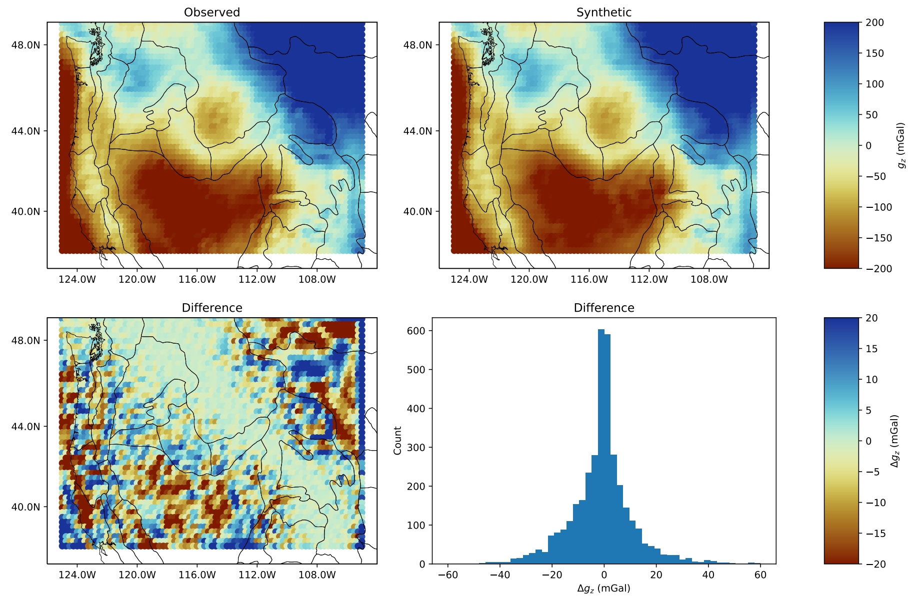

Figure 5: Plots of observed gravity signal, modelled gravity signal, difference in map view and histogram of the differences.

Figure 5 shows the observed and modelled gravity data, the difference between the two and a histogram of the differences. We can see a very good agreement between observed and synthetic values. In the central region of the model the residual is small and does not show significant correlated structure. Towards the boundaries of the model, e.g. in the north-eastern corner, we can identify regions of consistently higher or lower predicted gravity values. Two factors are responsible for this: i) The measured gravity values in these regions are large, so relatively speaking the residual is still less than 10 % ii) At the boundaries of the inversion domain, the flat Earth approximation used in the modelling becomes significant and this is reflected in the errors as explained above. However, in the central region the agreement is excellent and thus our conclusions are not impacted by these slightly larger discrepancies.

To further confirm that the agreement is excellent in critical regions, I show a zoomed view around the Yellowstone hotspot in Figure 6. Here the residual pattern appears largely random and the difference between observed and synthetic data is limited to ± 5 mGal which is compatible with the uncertainty of the data. I therefore conclude that the grav-

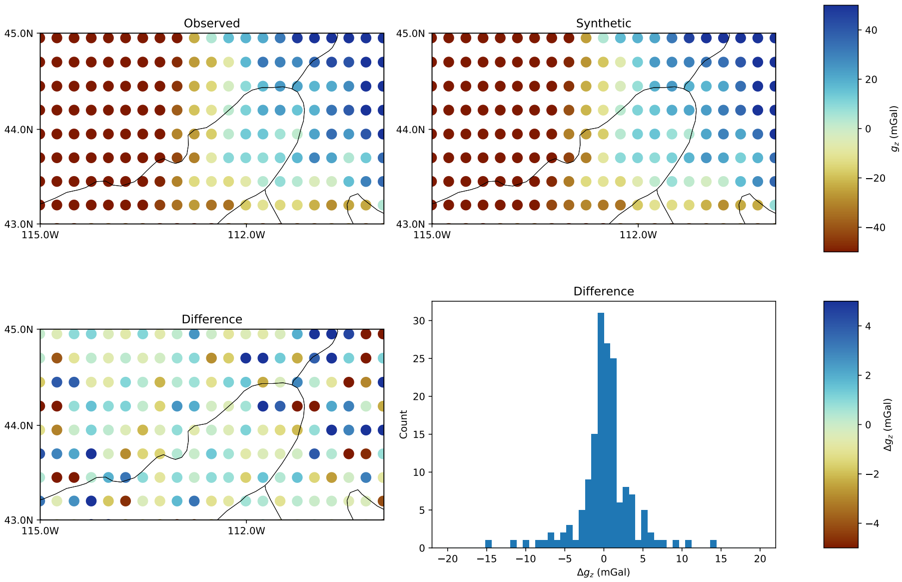

Figure 6: Same information is in Figure 5, but zoomed on the main region of interest around the Yellowstone hotspot.

ity data in the central region of the model are fit to a degree commensurate with the data quality and forcing a significantly better fit would likely result in inversion artefacts due to fitting noise.

For MT, the data misfit of each of the four components of impedance on a per-site basis is shown in Figure 7. As observed for the gravity data, at the majority of stations the misfit is compatible with the error assumptions (RMS around 1). Some isolated sites show higher misfit for individual components in the central region of the array and there appears to be a cluster of sites near the north-eastern corner of the measurement array where the Z_{xy} component exhibits higher misfit. Looking at individual curves in this area (see file mtfit.pdf in directory Data Fit), this is misfit is related to small discrepancies at the longest period MT data (corresponding to the deepest part of the model). Overall even for these sites the fit of the synthetics to the observed data is satisfactory and the difference is probably a result of large-scale structures outside the array influencing the sites at the boundary of our study area. It is unlikely though that the inversion models are significantly affected by this.

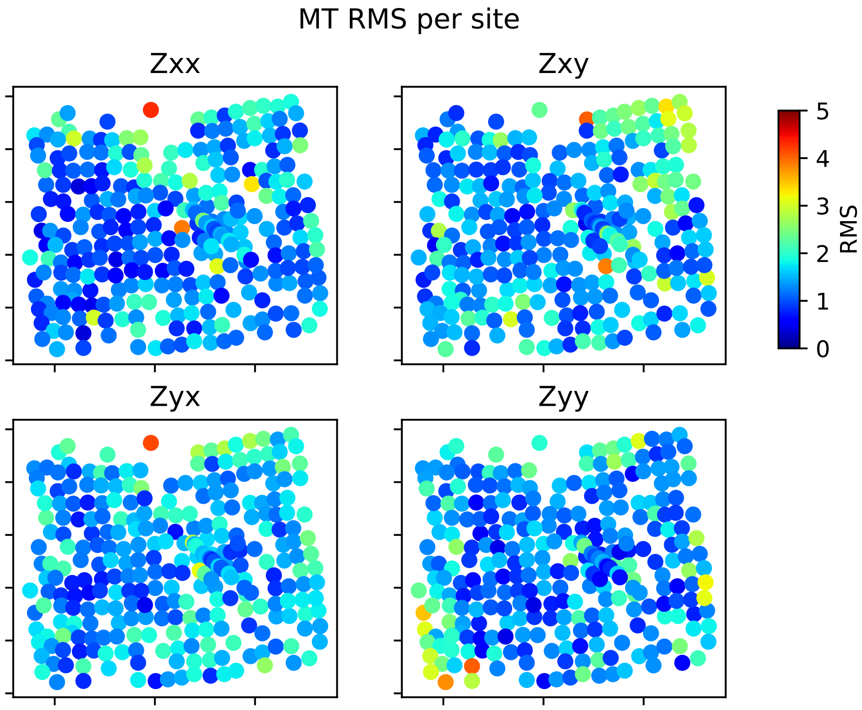

Figure 7: Misfit for the four components of impedance at each site.

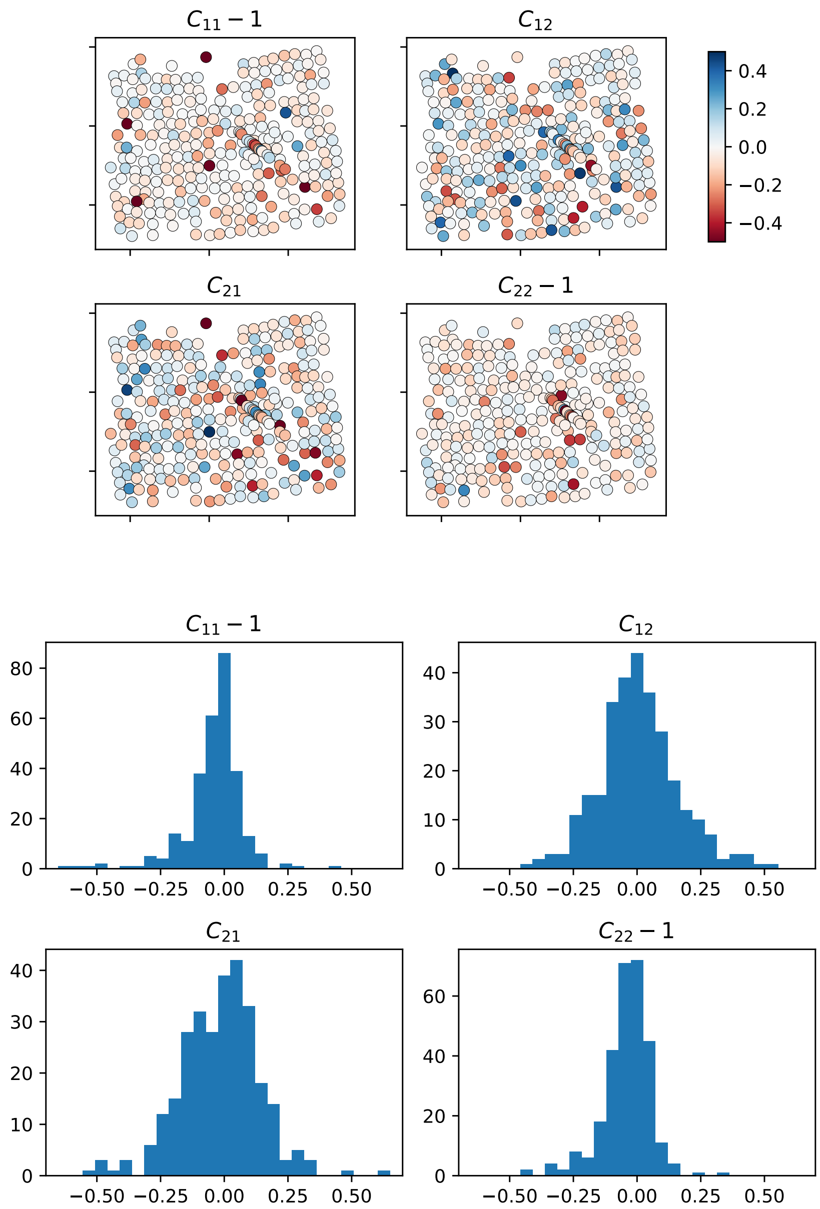

Figure 8: Deviation of the estimated distortion from an identity matrix (no distortion) for each component and site (top four panels) and as histograms (bottom four panels).

In addition to creating a conductivity model, the inversion also estimates the amount of galvanic distortion at each site. A detailed description of the method is given in Avdeeva et al. (2015), its robustness and a comparison of different strategies is shown in Moorkamp et al. (2020). The joint inversion follows the successful strategy presented in Moorkamp et al. (2020): The initial iterations are run without distortion correction and high regularization until a reasonable match between synthetics and observations is reached. Then distortion correction is enabled with a high distortion regularization and model regularization and distortion regularization are successively reduced until a good fit is reached.

Figure 8 shows information on the final distortion elements. I plot the deviation of the four elements of the distortion matrix **C** from the identity matrix (corresponding to no distortion). Overall, the estimated distortion is relatively low compared to other datasets Moorkamp et al. (2020). Sites with high distortion are isolated and scattered indicating that distortion does not mask significant structures Avdeeva et al. (2015). Furthermore, the four histograms are centered around zero deviation from the identity matrix and approximately symmetric. This shows that there is no average distortion across the array. A skewed distribution of distortion could be taken as an indicator that the inversion model is too resistive or too conductive on average and this discrepancy is counteracted by the distortion. I do not see any indication of this for the joint inversion model suggesting that the estimated distortion is related to small scale structure below the resolution of the inversion.

4 Sensitivity tests

In order two investigate to which degree the crustal conductivity and crustal density structures are required by the data, I conduct two sensitivity tests: i) Regions with high density and high conductivity in the crust are replaced with a lower density commensurate with the main trend of the parameter relationship (Figure 3 in the main manuscript). ii) High lower crustal conductivity is replaced with moderate conductivity (100 Ωm). These tests will demonstrate which aspects of the data are sensitive to the main structures of interest and demonstrate that the recovered contrast between high density conductors and low density conductors is not an inversion artefact.

Figure 9 shows a comparison between the inversion model (left) and the modified model (right) at a depth of 33 km. In the modified model all high density regions co-

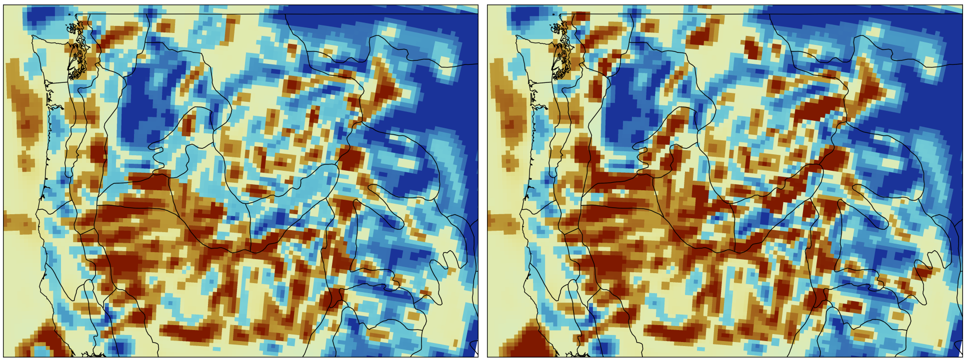

Figure 9: Comparison between the preferred density model (left) and the modified model (right) at a depth of 33 km to test the sensitivity to the high density structure.

inciding with conductors have been replaced with densities compatible with the main trend of the relationship. This change is most easily visible along the northern boundary of the Snake River Plain. Note that regions that exhibit high density but no enhanced conductivity remain unchanged. The corresponding synthetic gravity data, observations and gravity misfit are shown in Figure 10. For clarity I concentrate on the eastern end of the Snake River Plain, but similar effects can be seen in all regions of the model where high density has been decreased. Compared to the fit of the inversion (see Figure 6), a significant discrepancy between observations and synthetic data can be observed. This can be most clearly seen in the histogram of misfit (lower right panel in Figure 9) which shows an offset of 5-10 mGal for many measurements and even exceeding 15 mGal for some. This indicates that such a model that attributes high conductivity in this area to fluids is not compatible with the observations.

The depth of the mid and lower crustal conductors matches the results of previous investigations Kelbert et al. (2012); Bedrosian & Feucht (2014); Meqbel et al. (2014) and thus the sensitivity tests performed in these studies apply also to the results presented here. I therefore focus specifically on the conductive structures that do not lie on the main trend of the parameter relationship. Figure 11 shows a comparison between the preferred resistivity model (left) and a modified model (right) where conductive structures associated with high density are replaced with moderate conductivity (100 Ωm). The main changes occur at depths between 20–40 km. All other structures in the model remain identical.

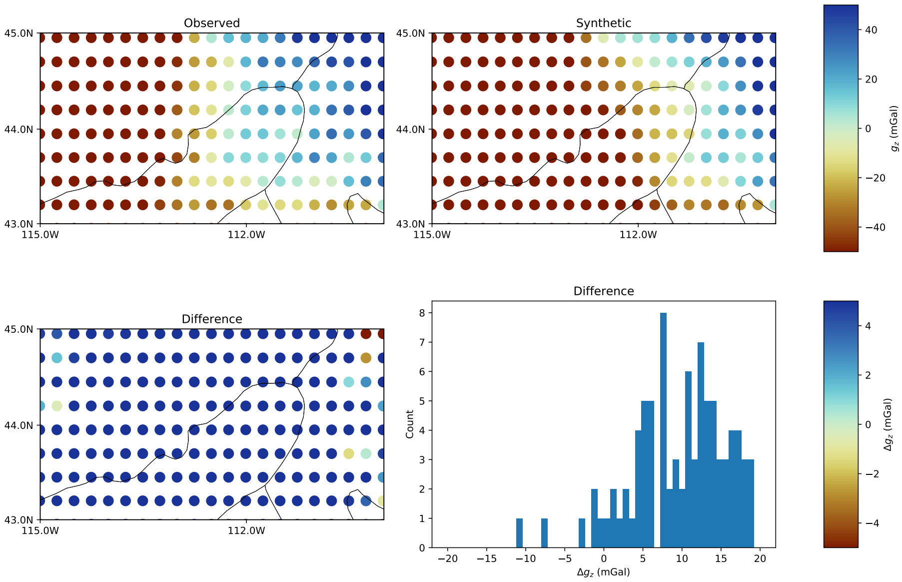

Figure 10: Observed and synthetic gravity data as well as residuals for the modified model without high density conductors.

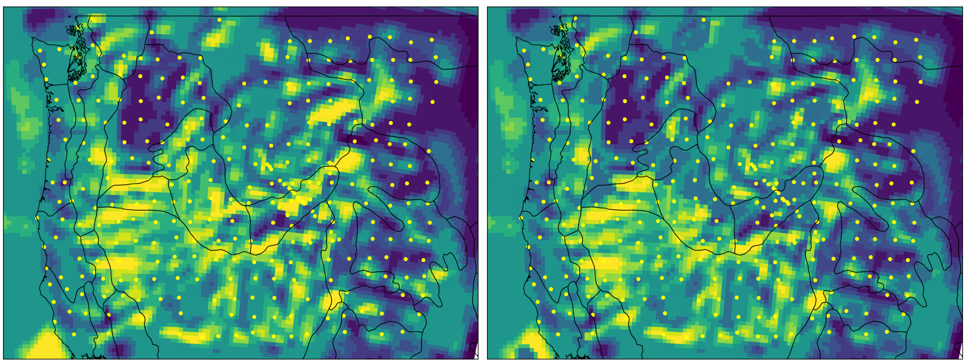

Figure 11: Comparison between the preferred resistivity model (left) and the modified model (right) at a depth of 33 km to test the sensitivity to the conductivity structure.

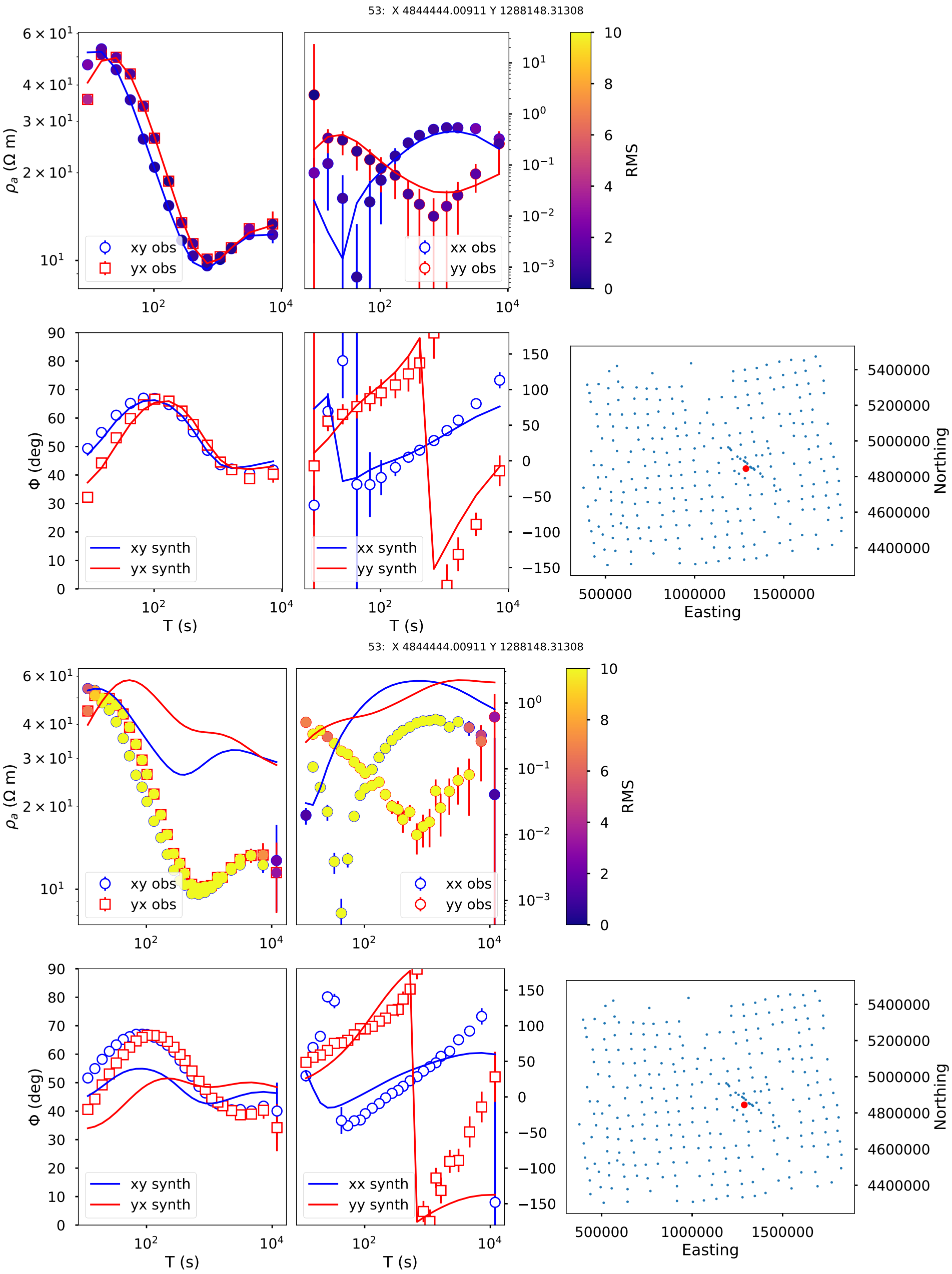

Figure 12: Fit of an exemplary site for the preferred model (top) and the modified model (bottom). The reduced conductivity in the lower crust results in a significantly increased misfit.

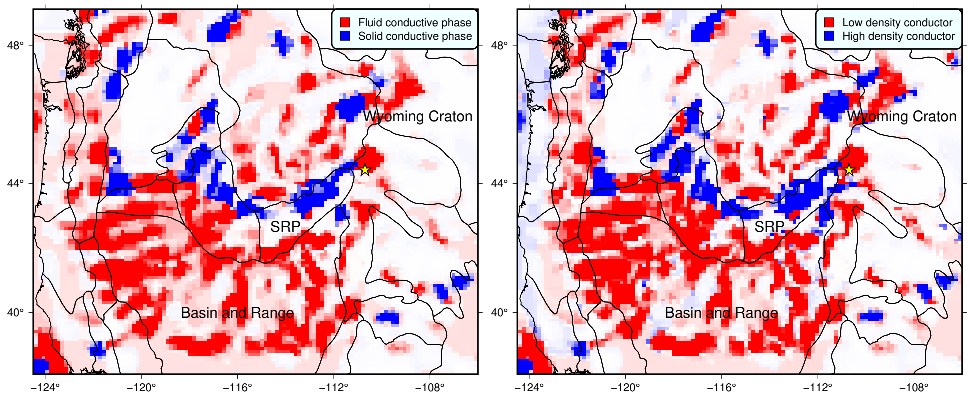

Figure 13: Comparison of inferred crustal conducitivity structure from our preferred model (left) and a joint inversion with gravity data derived from XGM2019 (right).

A comparison of MT sounding curves and the predicted response of the two models is shown in Figure 12. While the preferred model fits the observations well across the measured frequency range, the modified model only achieves a reasonable fit at short periods. This corresponds to the shallow part of the model which have not been altered. At periods > 100 s the synthetic data deviate from the observations for a four impedance components. Similar effects can be observed at other stations and thus the modified model is not a viable explanation for the observations.

5 Alternative inversion results

A possible source of uncertainty for the inversion results is the processing applied to the gravity to remove the effect of topography and crustal thickness variations. The processing is performed based on an established workflow, so the risk of topographic effects bleeding into the inversion model is small. Still, it is important to verify that the results are robust to variations in the processing of the gravity data. I therefore perform an alternative inversion with gravity data based on the XGM2019 model. For this inversion I download the bouguer corrected gravity data from the ICGEM portal and do not perform additional processing. All other parameters (magnetotelluric data, weighting etc.) remain identical to the preferred inversion result.

Figure 13 shows a comparison between the inferred crustal conductivity from our preferred model (left panel) and the joint inversion with XGM2019 (right panel). Overall, the two results are very similar and the inferred high density conductors are imaged in the same locations. There are some differences in the detailed geometries of these structures. For example, with XGM2019 the inversion retrieves a more extensive region of high density conductors along the south-eastern border of the Snake River plain. Other, more minor, differences can be identified in other parts of the model. However, none of these have significant impact on the interpretation or conclusions put forward in the main manuscript.

6 Other files contained in this release

In addition to this document I provide the model files and data files used for the inversion, python scripts to plot these files and detailed plots. These are organized in different directories which will be described below. Each directory contains the original files in NetCDF (`https://www.unidata.ucar.edu/software/netcdf/`) format (ending in .nc). These can be used with the provided python scripts (ending in .py) to produce Figures in .pdf format (included in the release) or for further analysis with other software such as MATLAB or modified python scripts.

6.1 Directory modelplots

This directory contains comprehensive plots of the preferred inversion model. The files *ewslices.pdf* and nsslices.pdf contain vertical slices through the joint resistivity-density model in East-West and North-South directions, respectively. *horslices_res.pdf* contains horizontal slices of resistivity and *horslices_dens.pdf* the corresponding densities. In addition the directory contains GeoTiffs for all horizontal slices that can be imported in GIS software or Google Earth. Here the name contains the depth to the top of slice in meters. All output files can be recreated with the four python scripts *ewslices.py*, *nsslices.py*, *horslices.py* and *horslices_dens.py* in the directory *Sources* which also contains the model files.

6.2 Directory Data Fit

This directory contains plots of the MT and gravity misfit for the preferred model. *gravfit.pdf* shows the fit to the gravity data over the whole area, while *gravfit_zoom.pdf* shows a version focused on the eastern Snake River Plain. The file *mtfit.pdf* shows oberved sounding curves and model predictions for all components of the MT tensor at each site.

References

Avdeeva, A., Moorkamp, M., Avdeev, D., Jegen, M., & Miensopust, M. (2015). Three-dimensional inversion of magnetotelluric impedance tensor data and full distortion matrix. *Geophysical Journal International*, *202*(1), 464–481.

Bedrosian, P. A., & Feucht, D. W. (2014). Structure and tectonics of the northwestern united states from earthscope usarray magnetotelluric data. *Earth and Planetary Science Letters*, *402*, 275–289.

Kelbert, A., Egbert, G., et al. (2012). Crust and upper mantle electrical conductivity beneath the Yellowstone Hotspot Track. *Geology*, *40*(5), 447–450.

Meqbel, N. M., Egbert, G. D., Wannamaker, P. E., Kelbert, A., & Schultz, A. (2014). Deep electrical resistivity structure of the northwestern US derived from 3-d inversion of USArray magnetotelluric data. *Earth and Planetary Science Letters*, *402*, 290–304.

Moorkamp, M., Avdeeva, A., Basokur, A. T., & Erdogan, E. (2020, 06). Inverting magnetotelluric data with distortion correction—stability, uniqueness and trade-off with model structure. *Geophysical Journal International*, *222*(3), 1620-1638. doi: 10.1093/gji/ggaa278

Müller, R. D., Sdrolias, M., Gaina, C., & Roest, W. R. (2008). Age, spreading rates, and spreading asymmetry of the world's ocean crust. *Geochemistry, Geophysics, Geosystems*, *9*(4).

Pail, R., Fecher, T., Barnes, D., Factor, J., Holmes, S., Gruber, T., & Zingerle, P. (2018). Short note: the experimental geopotential model xgm2016. *Journal of geodesy*, *92*(4), 443–451.

Szwillus, W., Afonso, J. C., Ebbing, J., & Mooney, W. D. (2019). Global crustal thickness and velocity structure from geostatistical analysis of seismic data. *Journal of Geophysical Research: Solid Earth*, *124*(2), 1626–1652.

Szwillus, W., Ebbing, J., & Holzrichter, N. (2016). Importance of far-field topographic and isostatic corrections for regional density modelling. *Geophysical Journal International*, *207*(1), 274–287.

Uieda, L., Barbosa, V. C., & Braitenberg. (2016). Tesseroids: Forward-modeling gravitational fields in spherical coordinates. *Geophysics*, *81*(5), F41–F48.